*Int. J. Electrochem. Sci.*, 16 **(2021)** Article ID: 210229, doi: 10.20964/2021.02.33

International Journal of
ELECTROCHEMICAL
SCIENCE
www.electrochemsci.org

# Electrochemical Impedance Spectroscopy Study on Using $Li_{10}GeP_2S_{12}$ Electrolyte for All-Solid-State Lithium Batteries

*Hongliang Li* [1], *Tong Zhang*[1], *Zi Yang* [1], *Yueli Shi*[1], *Quanchao Zhuang*[1,*], *Yanhua Cui*[2,*]

[1] School of Materials Science and Engineering, China University of Mining and Technology, Xuzhou 221116, China
[2] Institute of Electronic Engineering, China Academy of Engineering Physics, Mianyang 621900, China
[*]E-mail: zhuangquanchao@126.com; cuiyanhua@netease.com

*Received:* 7 May 2020 / *Accepted:* 14 December 2020 / *Published:* 31 December 2020

The electrochemical impedance spectroscopy (EIS) technique has been widely used for analysing lithium battery systems, especially to determine kinetic and transport parameters, understand reaction mechanisms, and study capacity fade mechanisms. In this work, the initial charge-discharge process of $LiCoO_2$@$LiNbO_3$/$Li_{10}GeP_2S_{12}$/Li (LLCO/LGPS/Li) and $LiNi_{0.5}Co_{0.2}Mn_{0.3}O_2$@$LiNbO_3$/$Li_{10}GeP_2S_{12}$/Li (LNCM523/LGPS/Li) batteries at different potentials was systematically investigated by EIS. During the lithium-ion insertion-removal process, the Nyquist plots of both LLCO/LGPS/Li and LNCM523/LGPS/Li batteries are composed of three parts, namely, two semicircles and an inclined line, which can be attributed to the interfacial impedance between the solid electrolyte and electrode, the charge transfer process, and the solid-state diffusion of the lithium-ion in the cathode with decreasing frequency, respectively. A proper equivalent circuit is proposed to fit the experimental EIS data and the variations in the interfacial resistance ($R_{if}$) between the solid electrolytes (SEs) and electrode. The charge transfer resistance ($R_{ct}$) along with the increase or decrease in the electrode polarization potential is quantitatively analysed in detail. Based on the experimental results, it has been revealed that, the increase in $R_{if}$ between the solid electrolyte and electrode may cause the capacity fade of all-solid-state batteries during charge-discharge.

**Keywords:** All-solid-state battery; Electrochemical impedance spectroscopy; $Li_{10}GeP_2S_{12}$ solid electrolytes; Interfacial resistance; Charge transfer resistance

## 1. INTRODUCTION

Since the launch of lithium-ion batteries into the market in 1991 [1], They have enjoyed widespread use in portable electronic devices for over two decades. Because lithium-ion batteries have the highest energy density of all commercially available batteries, they have been increasingly studied for realizing their use as large power sources, such as those used in electric vehicles (EVs) and

renewable energy storage systems [2]. However, there are many safety problems attributed to their combustible organic liquid electrolytes, and these problems become more serious when increasing the size of batteries for use in EVs, renewable energy storage and other particular applications that run at a high temperature (such as military applications). Inorganic solid-state electrolytes (SSEs), such as ceramic electrolytes which are nonflammable, are perfect answers to this safety issue [3]. Replacing the organic liquid electrolyte with SSEs will greatly increase apparatus safety and solve one of the few remaining obstacles hindering the even wider application of Li-ion technology. Moreover, SSEs also have many other advantages, such as superior electrochemical stability, thermal stability and mechanical stability, along with the important absence of leakage, and potential for battery miniaturization [4]. Therefore, all-solid-state lithium batteries (ASSLBs) with nonflammable inorganic solid electrolytes, as an alternative to conventional inflammable organic liquid electrolytes, are next generation batteries with very minimal risks in regard to leakage and explosion [5-8].

Despite their high safety, the power densities, or high-rate capabilities of ASSLBs remain poor hindering their practical use. The low ionic conductivities of SSEs and large interfacial impedances between electrolytes and electrodes have been the principal reasons for the poor high-rate capabilities of ASSLBs. To overcome these problems, in addition to searching for new materials to maximize the conductivity of SSEs [9-11]. It is extremely important to better comprehend the mechanism for fast ionic transport in SSEs, and the charge transfer reaction at the electrode/electrolyte interface. Unfortunately, searching for new materials and investigating their ionic conduction mechanisms to maximize the conductivity of SSEs seem to draw much attention from current pure research in the ASSLB field[12-14], and there is relatively few scientific studies on the the charge transfer reaction at the electrode/electrolyte interface to minimize the interfacial impedances [15-19]. The charge transfer reaction may be main barrier for developing high-performance solid-state batteries for electric vehicles and renewable energy storage systems [20].

At present, the $Li_2S$-$P_2S_5$ system sulfide solid electrolyte is considered to be one of the best electrolyte materials for ASSLBs [21, 22], because sulfide solid electrolytes tend to inherently show fast ionic conduction as a result of the high polarizability of sulfide ions. Furthermore, these sulfide materials are soft and deformable enough to form good interfacial connections, while showing low grain boundary resistances without sintering [9, 10]. The sulfide solid electrolyte $Li_{10}GeP_2S_{12}$ (LGPS) exhibits a high ionic conductivity of $1.2\times10^{-2}$ S cm$^{-1}$ at room temperature [23], and the $70Li_2S•30P_2S_5$ glass-ceramic has been demonstrated to have a high ionic conductivity of to $1.7\times10^{-2}$ S cm$^{-1}$ at room temperature [24]. Compared to those of organic liquid electrolytes, these sulfide solid electrolytes have superior ionic conductivities, making the commercialization of high-performance ASSLBs very promising. Electrochemical impedance spectroscopy (EIS) constitutes a powerful diagnostic technique for studying both the bulk transport properties of a material and the electrochemical reactions on its surface. One main advantage of EIS is that it can separate a complicated reaction into elementary processes based on differences in time constants, providing insights into the electrochemical processes, that occur inside the cells during operation [25]. Furthermore, EIS is also a powerful means for in situ measurement and does not require disassembly of the battery. Thus, EIS has been applied in the field of lithium-ion battery analysis and diagnosis in the past two decades [26-31]. To our knowledge, ASSLBs using the $Li_{10}GeP_2S_{12}$ electrolyte have not been researched systematically by EIS. In this

study, we prepared an all-solid-state cell with $LiNbO_3$-coated $LiCoO_2$ (LLCO) and $LiNbO_3$ coated $LiNi_{0.5}Co_{0.2}Mn_{0.3}O_2$ (LNCM523) as the cathode, LGPS as the electrolyte and Li metal as the anode. The electrochemical performance of the cell was evaluated using a charge-discharge test, and the initial charge-discharge processes of LLCO/LGPS/Li and LNCM523/LGPS/Li ASSLBs were investigated by EIS.

## 2. EXPERIMENTAL

### *2.1. Materials Preparation*

Oxide coatings are an effective way to achieve low-resistance interface at cathode using 4 V-class oxide electrodes according to previous reports [32,33]. Thus, the $LiCoO_2$ (LCO) or $LiNi_{0.5}Co_{0.2}Mn_{0.3}O_2$ (NCM523) particles were coated with $LiNbO_3$. The $LiNbO_3$ coatings were obtained by the sol-gel method. In a typical synthesis, niobium (V) ethoxide (99.9%, Alfa Aesar), lithium ethoxide (99.9%, Aladdin) and LCO (99%, Xiamen Tungsten Co) were used as the starting materials. First, 44.9 mg niobium (V) ethoxide and 7.3 mg lithium ethoxide were added to a 20 ml ethanol acetonitrile solvent and stirred for 2 h at room temperature. After that, 1 g of LCO was added to the above solution. The solution was continuously stirred for 6 h at room temperature to ensure sufficient reaction and then dried at 60 °C to eliminate the ethanol solvent. Finally, the as-prepared precursor powder was heated at 400 ℃ for 1 h in flowing oxygen to obtain $LiNbO_3$ coated LCO (LLCO). The preparation method of the $LiNbO_3$ coated $LiNi_{0.5}Co_{0.2}Mn_{0.3}O_2$ (LNCM523) was the same as that mentioned above.

The LGPS solid electrolyte was prepared by a simple solid phase method. Reagent-grade $Li_2S$ (99.9%, Aladdin), $GeS_2$ (99.9%, Aladdin) and $P_2S_5$ (99.9%, Aladdin) crystalline powders were used as starting materials. These materials were weighed to achieve a molar ratio of $Li_2S$: $P_2S_5$: $GeS_2$ = 5:1:1, sealed in a $ZrO_2$ pot and mixed for 30 min using a high-energy vibrating mill. The mixed powder was pressed into pellets at 280 MPa and transferred to a tube furnace, where the pellets were heated at 550 ℃ for 8 h. The composite cathode powders were prepared with the as-prepared LGPS, LLCO (or LNCM523) and carbon black, which were ball-milled at 450 rpm for 2 h at a mass ratio of 60:30:10. All preparations and sample treatments were performed in an Ar atmosphere.

### *2.2 Materials characterizations*

The structural characterizations of the LGPS were analysed by X-ray diffraction (XRD) using an X-ray diffractometer (Bruker D8 Advance, Germany) with a Cu Kα radiation (λ=1.54 Å) in a 2-theta ranging of 10 to 70° at a scan rate of 5° $min^{-1}$. Scanning electron microscopy (SEM, Hitachi S-4800) and elemental mapping were used to observe the microscopic morphology of the sample.

### *2.3 Electrochemical measurements*

ASSLBs were prepared in a dry Ar-filled glove box. For the ionic conductivity measurements,

electrolyte pellets were formed by cold pressing 150 mg of the LGPS in a stainless-steel mould (Φ13 mm) under 360 MPa for 2 min. Stainless-steel (SS) disks were attached on both faces of the pellets as blocking electrodes, and impedance was recorded between 25 and 120 °C using a blocking battery SS/LGPS/SS cell. The assembly of SS/LGPS/Li cell is similar to that of the SS/LGPS/SS, and SS disks were attached on one side of the electrolyte and lithium metal on the other side and then encapsulated in a CR2025 battery case.

For the assembly of ASSLBs, 4.5 mg of the composite cathode powder was uniformly distributed to an SS mould (Φ13mm), then 120 mg of the LGPS powder was uniformly distributed over the positive electrode material, and cold pressed at 360 MPa for 2 min. After that, the pellet was removed, a 12-mm-diameter lithium piece was attached to another side of the electrolyte, and then packaged in a battery case (CR2025). The charge-discharge curve was measured by a workstation system (CT2001A, LAND) at room temperature under a rate of 0.05 C, and impedance was recorded at a cut-off voltage ranging from 3.0 to 4.2 V (vs. $Li/Li^+$) for the LLCO/LGPS/Li battery and 2.7-4.3 V (vs. $Li/Li^+$) for the LNCM523/LGPS/Li battery.

EIS was performed using an electrochemical workstation (Autolab PGSTAT302N) over a frequency range of 10 MHz-0.01 Hz, and an applied AC perturbation signal of 5 mV. Cyclic voltammetry (CV) was conducted on an electrochemical workstation (CHI660E, Shanghai Chenhua Instrument Factory) using a semi-blocking Li/LGPS/SS battery to obtain the electrochemical window.

## 3. RESULTS AND DISCUSSION

Fig. 1a shows the XRD patterns of LGPS, LLCO and LNCM523 prepared in this work. The position and relative peak intensity of the XRD peak of the composite materials are consistent with the calculated results. The main characteristic diffraction peaks appear at 2θ = 20°, 26.7°, and 29.4° for LGPS, corresponding to a tetragonal shape with a space group of $P4_2/nmc$; this result matches well with previous reports [23, 34, 35], indicating that the LGPS solid electrolyte is successfully synthesized. Compared with the untreated materials, the main peaks of LLCO and LNCM523 show no change, and the correlation peak of $LiNbO_3$ does not appear, displaying that there is no impact on the structure of LCO and NCM523 during the coating process and that the coating layers are thin. To further illustrate that the surface of NCM523 is successfully coated with $LiNbO_3$, the NCM523 and LNCM523 samples were characterized using SEM. As shown in Fig. 1b and c, the NCM523 sample contains micron-sized particles with uneven sizes, and the surface of the sample particles is smooth. However, the surface of the LNCM523 sample is rough, and the particle profile of the sample is blurred in comparison with that of the NCM523 sample, demonstrating that the surface of the LNCM523 sample is successfully coated with a thin layer of $LiNbO_3$. In addition, we performed a mapping test on LNCM523 as shown in Fig. 1d. The results show that the Nb and O are distributed homogeneously throughout the particles, further demonstrating that the surface coating is relatively uniform.

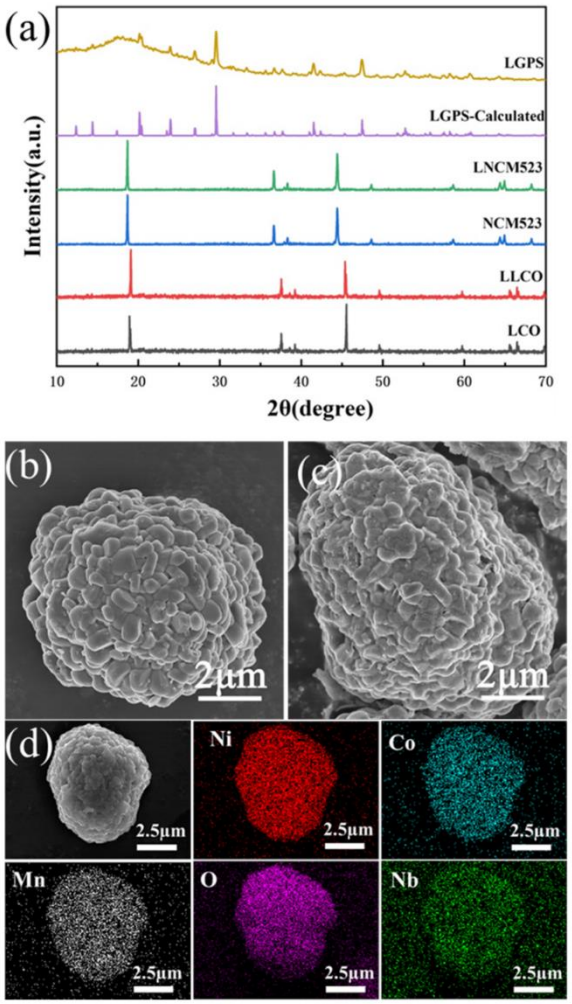


**Figure 1.** (a) X-ray diffraction patterns of LGPS, LNCM523 and LLCO; SEM images of (b) NCM523 and (c) LNCM523; and (d) mapping images of LNCM523.

As shown in Fig. 2a, the impedance spectra of the SS/LGPS/SS cell show a small compressed semicircle in the high frequency region and a straight line in the low frequency region. The ionic conductivity of LGPS was calculated from the impedance plots, and it was simply taken as the resistance values corresponding to the intercept of the linear fit of the straight line with the x-axis (e.g., when the imaginary part is equal to zero) [36]. The ionic conductivity of LGPS at room temperature is $2.02\times10^{-3}$ S cm$^{-1}$, and it can be seen that, the ionic conductivity of the LGPS solid electrolyte conforms to the Arrhenius equation:

$$\sigma = A\exp(-E_a/KT) \qquad (1)$$

where $E_a$ represents the activation energy, $T$ represents the absolute temperature, $k$ represents the Boltzmann constant, and $A$ represents the pre-exponential factor. An activation energy of $E_a$ =29.8 kJ mol$^{-1}$ for the ionic conduction of LGPS is determined from the Arrhenius plot (Fig 2b). In regard to the SS/LGPS/Li cell, there are deposition peaks (at 0 V) and stripping peaks (at 0.5 V) for lithium (Fig. 2c). No obvious peaks are detected in the range of 0 to 6V, which indicates that there is no redox

reaction at the LGPS/Li interface; this result indicates that the LGPS electrolyte is stable when in contact with the lithium anode in the voltage range of 0 to 6 V，which is consistent with that reported in the literature [23,37] .

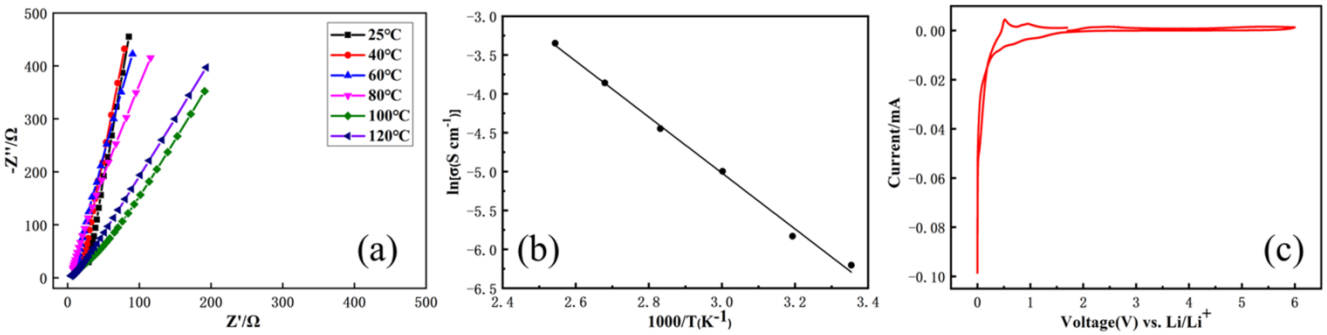


**Figure 2.** (a) Nyquist plots of the SS/LGPS/SS cell measured at different temperatures; (b) Arrhenius conductivity plots of LGPS; and (c) cyclic voltammetry curve of the SS/LGPS/Li cell.

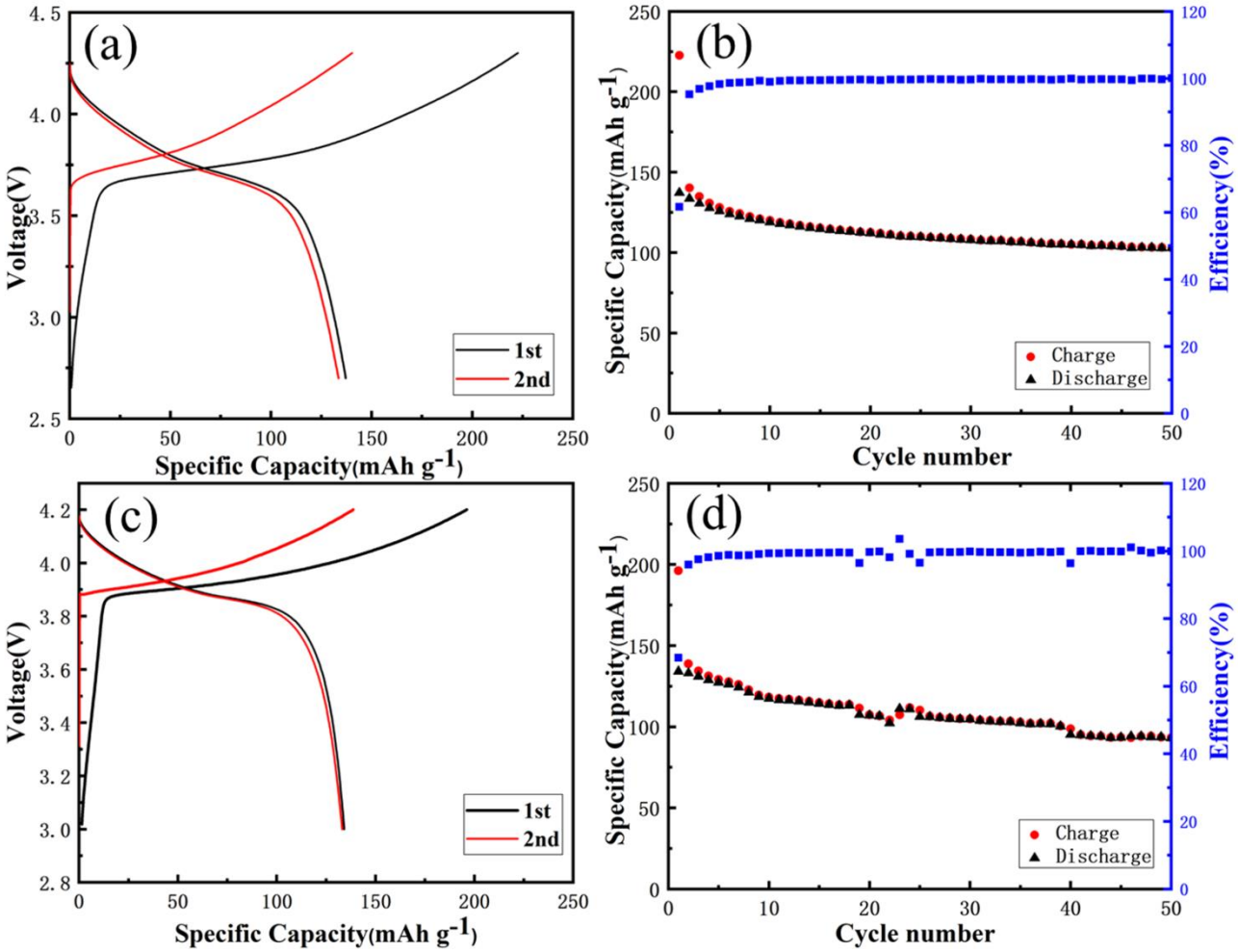


**Figure 3.** (a) Charge-discharge curves and (b) cycling performance curves of the LNCM523/LGPS/Li all-solid-state battery; and (c) charge-discharge curves and (d) cycling performance curves of the LLCO/LGPS/Li all solid-state battery.

Two types of solid-state batteries, LNCM523/LGPS/Li and LLCO/LGPS/Li, were fabricated and their electrochemical performance was investigated by charge-discharge tests. As shown in Fig. 3a and b, the initial discharge capacity of the LNCM523/LGPS/Li battery is 137.2 mAh $g^{-1}$ and the first coulombic efficiency is 61.6%; the coulombic efficiency increases to 95.2% in the 2nd cycle. After the 26th cycle, the coulombic efficiency is stable at approximately 99.7%. After the 50th charge-discharge cycle, the discharge capacity of the battery decreases to 102.8 mAh $g^{-1}$, and the capacity retention remains at 74.9%. Similarly, the LLCO/LGPS/Li cell shows an initial discharge capacity of 134.2 $mAhg^{-1}$ and a discharge capacity of 93.1 mAh $g^{-1}$ after the 50th cycle with a capacity retention of 69.4% which is lower than that of the LNCM523/LGPS/Li cell (Fig.3c and d). Table 1 shows the representative electrochemical performances of the ASSLBs, and it is evident that the cells we prepared in this article have relatively excellent electrochemical performance compared with similar cells reported in the literature [38-41].

**Table 1.** Representative electrochemical performances of ASSLBs

| Cell structure | Testing conditions | Performance | Ref. |
|---|---|---|---|
| $LiCoO_2$@$LiNbO_3$/$Li_{10}GeP_2S_{12}$/Li | 3.0~4.2V,0.05C,25℃ | 93.1 mAh $g^{-1}$ after 50th cycle | This article |
| $LiNi_{0.5}Co_{0.2}Mn_{0.3}O_2$@$LiNbO_3$/$Li_{10}GeP_2S_{12}$/Li | 2.7~4.3V,0.05C,25℃ | 102.8 mAh $g^{-1}$ after 50th cycle | This article |
| $LiCoO_2$@$LiNbO_3$/$Li_{10}GeP_2S_{12}$/In | 1.9~3.6 V, 1.4 mA $g^{-1}$, 25 ℃ | > 120 mAh $g^{-1}$ after 8th cycle | [38] |
| $LiMn_2O_4$/80$Li_2S$-20$P_2S_5$ /In | 3~4.6 V, 0.064 mA $cm^{-2}$, 25 ℃ | 54mAh $g^{-1}$ after 50th cycle | [39] |
| $LiNi_{0.5}Mn_{1.5}O_4$/$Li_{10}GeP_2S_{12}$/Li | 3.5~5 V, 7.3 mA $g^{-1}$, 25℃ | 89mAh $g^{-1}$ for 1st cycle | [40] |
| $LiNi_{0.8}Co_{0.1}Mn_{0.1}O_2$/β-$Li_3PS_4$/Li-In | 2.0~3.7 V, 0.1~1C, 25 ℃ | 81mA h $g^{-1}$ after 50th cycle | [41] |

To further analyse the interfacial compatibility between the electrolyte and electrode, EIS was carried out. For the LNCM523/LGPS/Li battery, EIS was recorded at a sequence of potentials from 2.7 to 4.3 V during the initial charge process and from 4.3 to 2.7 V during the initial discharge process. In Figs. 4 and 5, the Nyquist plot of the LNCM523/LGPS/Li battery consists of a small semicircle corresponding to the high frequency region and an inclined line corresponding to the low frequency region at an open circuit potential (OCP) of 2.7 V. With increasing potential, the small semicircle corresponding to the high frequency region hardly changes during the initial charge process. However, the inclined line corresponding to the low frequency region is strongly potential dependent, showing an increasing tendency to move towards the real axis and finally becoming a semicircle in the medium frequency region and a straight line in the low frequency region at 3.7 V when lithium ions begin to deintercalate from the cathode; this result indicates that the inclined line corresponding to the low frequency region represents the blocking character of the non-lithiated electrode at the equilibrium potential because of the large charge transfer resistance coupled with double capacitance while the semicircle corresponding to the medium frequency region should be ascribed to the charge transfer step[29,30]. Correspondingly, the Nyquist plots clearly consist of three parts: a small semicircle in the high-frequency region, a semicircle in the medium-frequency region and a Warburg-type element in the low-frequency region. When potential further increases to 4.3 V, the impedance characteristics of

the cell do not change during the charge process, but follow a converse pathway during the initial discharge process.

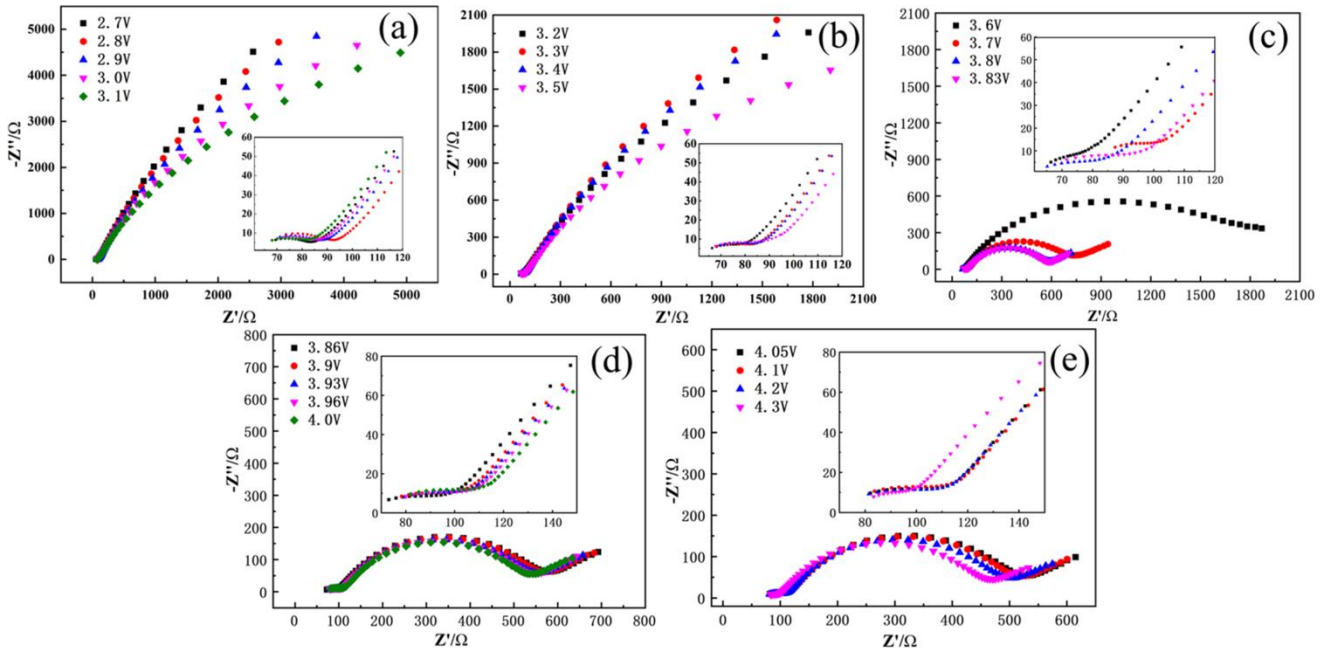


**Figure 4.** Nyquist plots of the LNCM523/LGPS/Li battery at a sequence of potentials from 2.7 to 4.3 V during the initial charge process.

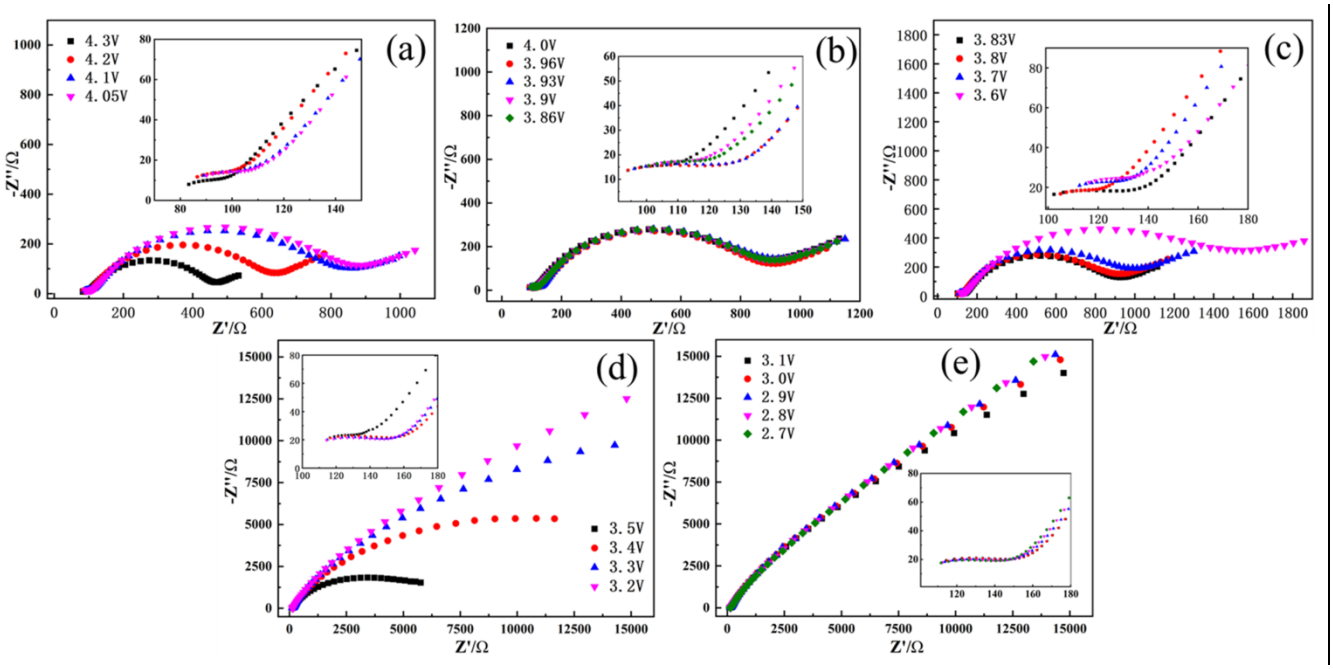


**Figure 5.** Nyquist plots of the LNCM523/LGPS/Li battery at a sequence of potentials from 4.3 to 2.7 V during the initial discharge process.

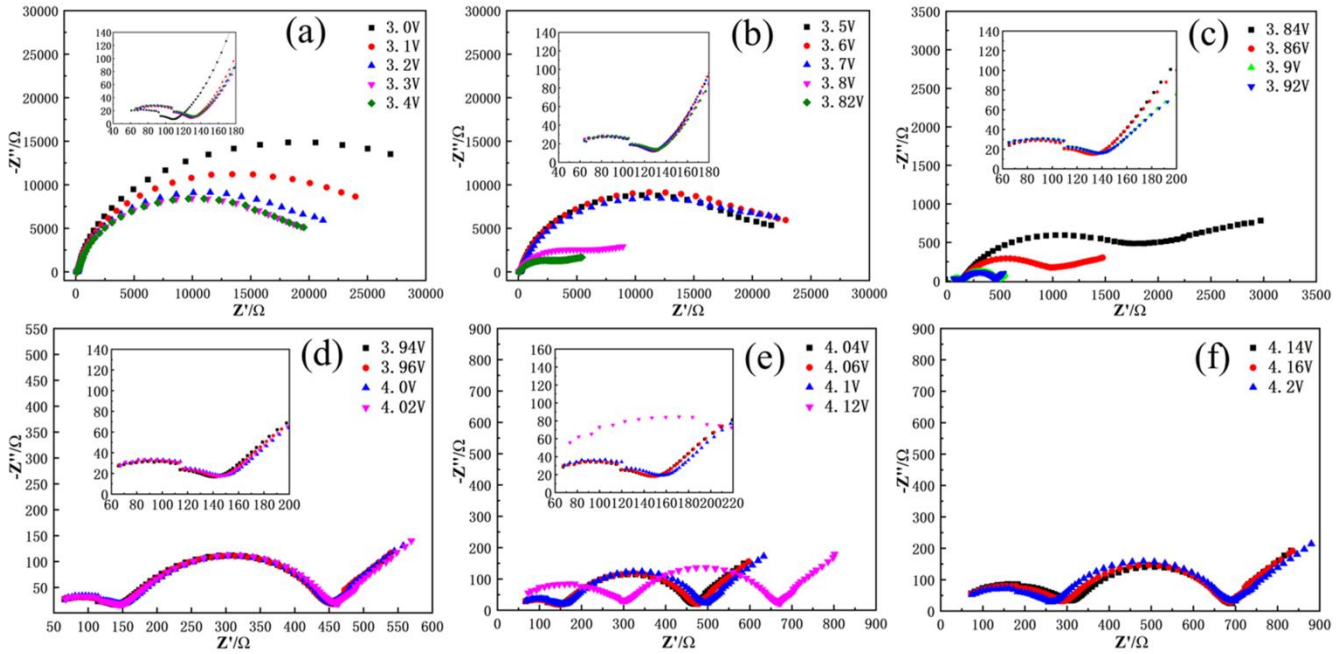


**Figure 6.** Nyquist plots of the LLCO/LGPS/Li battery at a sequence of potentials from 3.0 to 4.2 V during the initial charge process.

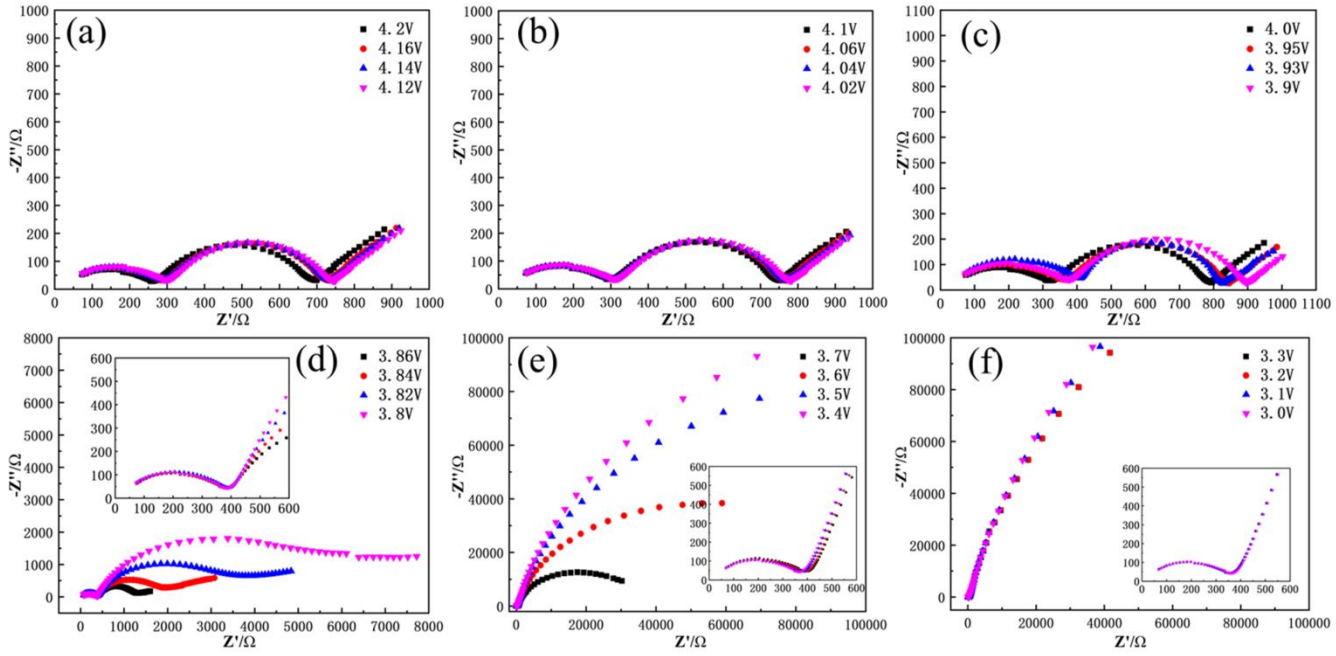


**Figure 7.** Nyquist plots of the LLCO/LGPS/Li battery at a sequence of potentials from 4.2 to 3.0 V during the initial discharge process.

According to previous studies on ASSLBs [42,43], the semicircle in the high-frequency region is ascribed to the interfacial resistance between solid electrolyte and electrode, the semicircle in the medium-frequency region is ascribed to charge transfer process as suggested in the above discussion, and the inclined line in the low-frequency region is attributed to solid-state diffusion of the lithium-ion

in the LNCM523 cathode. For the LLCO/LGPS/Li cell, the impedance characteristics are similar to those of the LNCM523/LGPS/Li cell during the initial charge-discharge process, as shown in Figs. 6 and 7.

Based on the above analysis, we provide the equivalent circuit to fit the Nyquist plots obtained from the experiment, as shown in Fig. 8. $R_b$ is the electrolyte bulk resistance, $R_{if}$ is the interfacial resistance between the solid electrolyte and electrode, $R_{ct}$ is the charge transfer resistance, and constant phase angle elements (CPEs) $Q_{if}$, $Q_{dl}$, and $Q_D$ represent the interfacial capacitance, electric double layer capacitance and diffusion resistance, respectively.

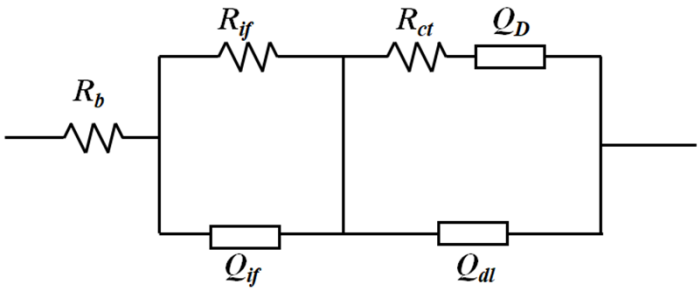


**Figure 8.** Equivalent circuit for the analysis of the first charge/discharge process of the LGPS all-solid-state battery

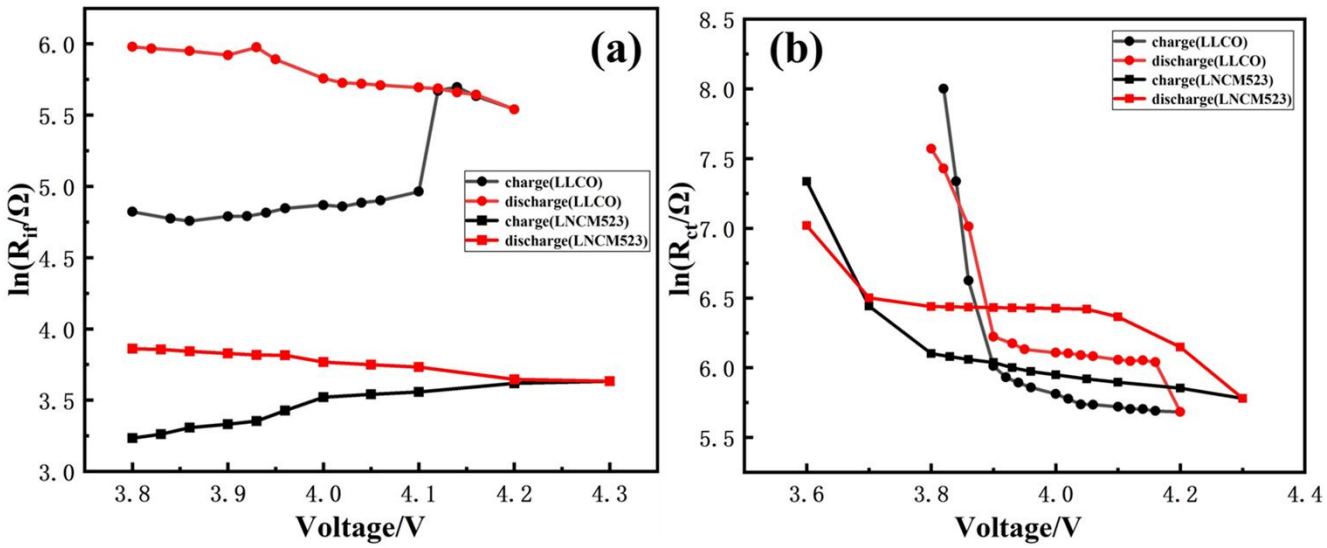


**Figure 9.** variations of (a) ln$R_{if}$ and (b) ln$R_{ct}$.

Fig. 9a shows the variation in ln$R_{if}$ as a function of the electrode potentials during the first charge/discharge process. $R_{if}$ increases slowly during the whole first charge-discharge process for the LNCM523/LGPS/Li cell. $R_{if}$ increases from 25.4 Ω at the OCP to 47.5 Ω after the initial charge process. In regard to the LLCO/LGPS/Li cell, $R_{if}$ increases slowly from 3.8 to 4.1 V during the initial charge process, and increases rapidly from 4.1 to 4.2 V, and then increases slowly during the initial

discharge process. $R_{if}$ increases from 124.2 Ω at the OCP to 254.6 Ω at the end of the initial discharge process.

Here we define $\eta = R_{if}(e)/R_{if}(0)$, where $\eta$ is the growth rate of $R_{if}$, $R_{if}(e)$ is the resistance of $R_{if}$ after the first discharge process and $R_{if}(0)$ is the resistance of $R_{if}$ at the OCP. For the LNCM523/LGPS/Li cell at voltages from 3.8 to 4.3 V, $\eta$ is 1.87, while $\eta$ is 2.05 for the LLCO/LGPS/Li cell at voltages ranging from 3.8 to 4.2 V. This result corresponds to the capacity retention rate of the LLCO/LGPS/Li battery being lower than that of the LNCM523/LGPS/Li battery, which shows that the interface between the SE LGPS and the electrode has great effect on the cycling performance of ASSLBs.

Fig. 9b shows the variations in ln$R_{ct}$. $R_{ct}$ satisfies the following classical equation [44]:

$$R_{ct} = \frac{1}{fFAk_s x^{0.5}(1-x)^{0.5}} \qquad (2)$$

Where $f$ represents the electrochemical constant ($f = F/RT$ where $F$ represents the Faraday constant, the $R$ represents gas constant and $T$ represents the absolute temperature), $A$ satisfies the total electroactive surface area, $k_s$ represents the heterogeneous rate constant, and $x$ represents the lithium ion insertion level. It can be seen from the equation. 2 that when $x > 0.5$, $R_{ct}$ decreases as $x$ decreases. At the OCP, $x$=1 for both the LLCO/LGPS/Li cell and the LNCM523/LGPS/Li battery, therefore, $R_{ct}$ of the LLCO/LGPS/Li battery and the LNCM523/LGPS/Li battery decreases as $x$ decreases, namely, the $R_{ct}$ of the LLCO/LGPS/Li and the LNCM523/LGPS/Li batteries decreases as the electrode polarization potential increase.s

As shown in Fig. 9b, during the first delithiation (or charge) process, $R_{ct}$ decreases as the electrode potential increases, which shows a reversible change process during the lithium insertion process and is in accordance with equation.2. In regard to the LLCO/LGPS/Li battery, the above result further demonstrates that the semicircle in the medium frequency region is classified as charge transfer process. Moreover, the trend of $R_{ct}$ of LNCM523/LGPS/Li battery is similar to that of the LLCO/LGPS/Li battery, showing that the influence of the charge transfer process on the capacity fade of ASSBs is insignificant.

## 4. CONCLUSION

In this paper, we synthesized $Li_{10}GeP_2S_{12}$ through high temperature solid phase method. The ionic conductivity of $Li_{10}GeP_2S_{12}$ at room temperature was $2.02\times10^{-3}$ S cm$^{-1}$ and its Ea calculated from Arrhenius plots was 29.8 kJ mol$^{-1}$. The first charge-discharge process of LLCO/LGPS/Li and LNCM523/LGPS/Li batteries at a range of potentials was researched by electrochemical impedance spectroscopy. The Nyquist plots of both LLCO/LGPS/Li and the LNCM523/LGPS/Li batteries were composed of three parts in the $Li^+$ insertion-removal process: a small semicircle in the high-frequency region, a semicircle in the medium-frequency region and an inclined line in the low-frequency region. The small semicircle corresponding to the high frequency region belongs to the interfacial impedance between the electrolyte and electrode, the semicircle corresponding to the medium frequency region is assigned to the charge transfer process, and the oblique line corresponding to the low frequency region relates to the solid-state diffusion of lithium-ion in the cathode. Based on the experimental results, it

has been revealed that, the increase in the interfacial impedance between the solid electrolyte and the electrode may be the main reason for the capacity fade of ASSLBs during the charge-discharge process. This result signifires that improving the electrochemical stability of the interface between the solid electrolyte and electrode should be one of the key methods to enhance the cycling performance of ASSLBs.

ACKNOWLEDGMENTS
This work was supported by the National Natural Science Foundation of China (No. U1730136); and the Fundamental Research Funds for the Central Universities (No. 2017XKQY062).

**References**

1. Y. Nishi, *J. Power Sources*, 100 (2001) 101.
2. V. Etacheri, R. Marom, R. Elazari, G. Salitra, D.J.E. Aurbach, *E. Science*, 4 (2011) 3243.
3. K. Murata, S. Izuchi, Y. Yoshihisa, *Electrochim. Acta*, 45 (2000) 1501.
4. P. Knauth, *Solid State Ion.*, 180 (2009) 911.
5. Y. Zhang, R. Chen, T. Liu, Y. Shen, Y. Lin, C.W. Nan, *ACS Appl. Mater. Interfaces*, 9 (2017) 28542.
6. A. Kuhn, V. Duppel, B.V.J.E. Lotsch, *E. Science*, 6 (2013) 3548.
7. P.L. Moss, G. Au, E.J. Plichta, J.P. Zheng, *J. Power Sources*, 189 (2009) 66.
8. S. Chen, D. Xie, G. Liu, J.P. Mwizerwa, Q. Zhang, Y. Zhao, X. Xu, X. Yao, *Energy Stor. Mater.*, 14 (2018) 58.
9. J.M. Whiteley, J.H. Woo, E. Hu, K.W. Nam, S.H. Lee, *J. Electrochem. Soc.*, 161 (2014) A1812.
10. Y. Kato, S. Hori, T. Saito, K. Suzuki, M. Hirayama, A. Mitsui, M. Yonemura, H. Iba, R. Kanno, *Nat. Energy*, 1 (2016) 16030.
11. P. Bron, S. Dehnen, B. Roling, *J. Power Sources*, 329 (2016) 530.
12. J.C. Bachman, S. Muy, A. Grimaud, H.H. Chang, N. Pour, S.F. Lux, O. Paschos, F. Maglia, S. Lupart, P. Lamp, L. Giordano, Y. Shao-Horn, *Chem. Rev.*, 116 (2016) 140.
13. R. Agrawal, R. K. Gupta, *J Mater Sci Technol.*, 34 (1999) 1131.
14. A. Chandra, A. Bhatt, A. Chandra, *J Mater Sci Technol.*, 29 (2013) 193.
15. C. Vinado, S. Wang, Y. He, X. Xiao, Y. Li, C. Wang, J. Yang, *J. Power Sources*, 396 (2018) 824.
16. F. Han, T. Gao, Y. Zhu, K.J. Gaskell, C. Wang, *Adv. Mater.*, 27 (2015) 3473.
17. W. Zhang, F.H. Richter, S.P. Culver, T. Leichtweiss, J.G. Lozano, C. Dietrich, P.G. Bruce, W.G. Zeier, J. Janek, *ACS Appl. Mater. Interfaces*, 10 (2018) 22226.
18. R. Xu, F. Han, X. Ji, X. Fan, J. Tu, C. Wang, *Nano Energy*, 53 (2018) 958.
19. A.C. Luntz, J. Voss, K. Reuter, *J. Phys. Chem. Lett.*, 6 (2015) 4599.
20. N. Ohta, K. Takada, L. Zhang, R. Ma, M. Osada, T. Sasaki, *Adv. Mater.*, 18 (2006) 2226.
21. Y. Wang, W.D. Richards, S.P. Ong, L.J. Miara, J.C. Kim, Y. Mo, G. Ceder, *Nat. Mater.*, 14 (2015) 1026.
22. D. Liu, W. Zhu, Z. Feng, A. Guerfi, A. Vijh, K. Zaghib, *Mater. Sci. Eng. B*, 213 (2016) 169.
23. N. Kamaya, K. Homma, Y. Yamakawa, M. Hirayama, R. Kanno, M. Yonemura, T. Kamiyama, Y. Kato, S. Hama, K. Kawamoto, A. Mitsui, *Nat. Mater.*, 10 (2011) 682.
24. Y. Seino, T. Ota, K. Takada, A. Hayashi, M. Tatsumisago, *Energ. Environ. Sci.*, 7 (2014) 627.
25. T. Osaka, D. Mukoyama, H. Nara, *J. Electrochem. Soc.*, 162 (2015) A2529.
26. J.A. Amani, T. Koppe, H. Hofsäss, U. Vetter, *Phys. Rev. Appl.*, 4 (2015) 044007.
27. Q.C. Zhuang, X.Y. Qiu, S.D. Xu, Y.H. Qiang, S.G. Sun, *Prog. Chem.*, 22 (2010) 1044.
28. Z. Siroma, T. Sato, T. Takeuchi, R. Nagai, A. Ota, T. Ioroi, *J. Power Sources*, 316 (2016) 215.
29. 29. Q.C. Zhuang, T. Wei, L.L. Du, Y.L. Cui, L. Fang, S.G. Sun, *J. Phys. Chem. C*, 114

(2010) 8614.
30. X.Y. Qiu, Q.C. Zhuang, Q.Q. Zhang, R. Cao, P.Z. Ying, Y.H. Qiang, S.G. Sun, *PCCP*, 14 (2012) 2617.
31. Q.C. Zhuang, J. Li, L.L. Tian, *J. Power Sources*, 222 (2013) 177.
32. N. Machida, J. Kashiwagi, M. Naito, T. Shigematsu, *Solid State Ion.*, 225 (2012) 354.
33. K. Okada, N. Machida, M. Naito, T. Shigematsu, S. Ito, S. Fujiki, M. Nakano, Y. Aihara, *Solid State Ion.*, 255 (2014) 120.
34. J. Hassoun, R. Verrelli, P. Reale, S. Panero, G. Mariotto, S. Greenbaum, B. Scrosati, *J. Power Sources*, 229 (2013) 117.
35. A. Kuhn, J. Köhler, B.V. Lotsch, *PCCP*, 15 (2013) 11620.
36. S. Boulineau, M. Courty, J.M. Tarascon, V. Viallet, *Solid State Ion.*, 221 (2012) 1.
37. F. Han, T. Gao, Y. Zhu, K. J. Gaskell, C. Wang, *Adv. Mater.* 2015,27(23), 3473.
38. N. Kamaya, K. Homma, Y. Yamakawa, M. Hirayama, R. Kanno, M. Yonemura, T. Kamiyama, Y. Kato, S. Hama, K. Kawamoto, A. Mitsui, *Nat. Mater*. 10 (2011) 682.
39. H. Kitaura, A. Hayashi, K. Tadanaga, M. Tatsumisago, *Solid State Ion.,* 192 (2011) 304.
40. G. Oh, M. Hirayama, O. Kwon, K. Suzuki, R. Kanno, *Chem. Mater.* 28 (2016) 2634.
41. R. Koerver, I. Aygün, T. Leichtweiß, C. Dietrich, W. Zhang, J.O. Binder,P. Hartmann, W.G. Zeier, J. Janek, *Chem. Mater.* 29 (2017)5574.
42. R.C. Xu, X.H. Xia, Z.J. Yao, X.L. Wang, C.D. Gu, J.P. Tu, *Electrochim. Acta*, 219 (2016) 235.
43. Q. Zhang, D. Cao, Y. Ma, A. Natan, P. Aurora, H. Zhu, *Adv. Mater.*, 31 (2019) 1901131.
44. M.D. Levi, K. Gamolsky, D. Aurbach, U. Heider, R. Oesten, *Electrochim. Acta*, 45 (2000) 1781.